

Deep Learning of Morphologic Correlations To Accurately Classify CD4+ and CD8+ T Cells by Diffraction Imaging Flow Cytometry

Lin Zhao, Liwen Tang, Marion S. Greene, Yu Sa, Wenjin Wang, Jiahong Jin, Heng Hong, Jun Q. Lu, and Xin-Hua Hu*



Cite This: *Anal. Chem.* 2022, 94, 1567–1574



Read Online

ACCESS |



Metrics & More

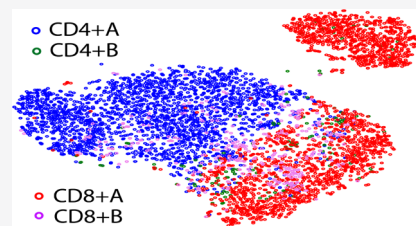


Article Recommendations



Supporting Information

ABSTRACT: The two major subtypes of human T cells, CD4+ and CD8+, play important roles in adaptive immune response by their diverse functions. To understand the structure–function relation at the single cell level, we isolated 2483 CD4+ and 2450 CD8+ T cells from fresh human splenocytes by immunofluorescent sorting and investigated their morphologic relations to the surface CD markers by acquisition and analysis of cross-polarized diffraction image (p-DI) pairs. A deep neural network of DINet-R has been built to extract 2560 features across multiple pixel scales of a p-DI pair per imaged cell. We have developed a novel algorithm to form a matrix of Pearson correlation coefficients by these features for selection of a support cell set with strong morphologic correlation in each subtype. The p-DI pairs of support cells exhibit significant pattern differences between the two subtypes defined by CD markers. To explore the relation between p-DI features and CD markers, we divided each subtype into two groups of A and B using the two support cell sets. The A groups comprise 90.2% of the imaged T cells and classification of them by DINet-R yields an accuracy of $97.3 \pm 0.40\%$ between the two subtypes. Analysis of depolarization ratios further reveals the significant differences in molecular polarizability between the two subtypes. These results prove the existence of a strong structure–function relation for the two major T cell subtypes and demonstrate the potential of diffraction imaging flow cytometry for accurate and label-free classification of T cell subtypes.



INTRODUCTION

Human T cells in vasculature and lymphoid organs consist of numerous functional subtypes and are essential to develop adaptive immunity against viral infections and certain tumors. Some forms of structure–function relation have been identified for T cells. Activation of CD4+ T cells has been found to correlate with changes in mechanical interaction with other cells,¹ and that of CD8+ T cells to correlate with changes in dry mass.² Past efforts on classification of T cell subtypes by morphologic differences, however, have achieved little success.^{3–6} Immunophenotyping is currently the only method to define and recognize subtypes of primary T cells in particular and primary lymphocytes in general.⁷ Among numerous subtypes of T cells, the CD4+ and CD8+ are the two major ones that exhibit high plasticity to differentiate into distinct effector forms, and their enumeration has been widely used as a clinical tool-of-choice to monitor immunodeficiency and effectiveness of therapy and vaccine.^{8–12} However, immunophenotyping relies on specific binding of endogenous and fluorochrome-conjugated CD antigens or markers to the surface receptors. The complex staining procedures and reagent costs add barriers to wide applications beyond the drawbacks of cytotoxicity, affinity variation, and fluorophore instability.^{13,14} Consequently, development of a label-free method for recognition of T cell subtypes can yield a valuable means for applications, where immunophenotyping is

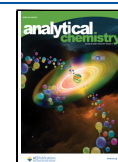
impractical. More importantly, critical insights can be gained from investigations on morphologic relations among T cells within the same subtype and between different subtypes defined by the surface CD markers to reveal the dependence of functions on their molecular interiors.

Previous imaging studies of human T cells' morphology, qualitative or quantitative, have been performed using methods of optical or electronic microscopy.^{2–6} These methods are based on acquisition of 2D images, which consist of pixels with intensity proportional to the numbers of photons or electrons emitted from the imaged cell following excitation. If a pixel or a set of neighboring pixels corresponds to one and only one local region of the cell, the smallest size of the region resolved by the image defines the spatial resolution of imaging, and the lower bound is limited by the diffraction nature of light or electron wavefields. Although the morphology of a cell is three-dimensional (3D), this principle of local imaging design leads to the 2D nature of morphological features extracted from the acquired images. To improve this, a stack of 2D images can be

Received: August 5, 2021

Accepted: December 27, 2021

Published: January 10, 2022



acquired from the same cell to reconstruct its 3D morphology by, for example, fluorescent confocal microscopy or diffraction tomography.^{15,16} The 3D reconstruction approach, however, is often disadvantaged by the very low throughput rate because both image stack acquisition and subsequent processing are time consuming.

Different from the local imaging methods, we have developed an approach of diffraction imaging and pattern analysis for classification of different particle types by recording coherent light scattered in the side directions, which is achieved using a single-shot method of polarization diffraction imaging flow cytometry (p-DIFC) for rapid assay of single cells.^{17–19} The p-DIFC method acquires one pair of cross-polarized diffraction images (p-DI) per cell by splitting the scattered light into s- and p-polarized components. Each pixel in a p-DI pair has its intensity determined by superposition of coherent wavefields emitted from all molecules in the imaged cell illuminated by a laser beam. Because the intracellular distribution of the refractive index (RI) determines the spatial distribution of the scattering light, one can regard each p-DI pair as a coded representation of the RI distribution homologous to the 3D morphology of cell. It is widely known that the type and spatial distribution of intracellular molecules determine RI distribution by their polarizability. Consequently, the diffraction pattern features learned from a p-DI pair carry rich information on morphology or molecular interiors for cell classification without reconstruction. Numerical modeling of light scattering by single cells verifies the cell assay capability of diffraction imaging.^{20–22} With machine learning of the diffraction patterns embedded in p-DI pairs, accurate and rapid classification has been demonstrated experimentally for various immortalized cancer cells including Jurkat T and Ramos B cells.^{23–28} However, the ability of the p-DIFC method to classify primary human T cells phenotyped by CD markers is unknown because these cells exhibit strong population heterogeneity in comparison to cell lines maintained in a controlled environment. Because CD4+ or CD8+ T cells comprise functional phenotypes of different cytokine profiles,²⁹ the study of T cell classification without immunofluorescent labels is a topic of ongoing research. Important questions remain unanswered such as if and how the T cell subtypes defined by CD markers have measurable differences in their morphology-related properties.

In this report, we present a study on the morphologic implication of CD4+ and CD8+ T cells isolated from fresh human splenocytes by acquisition and analysis of p-DI pairs. A novel algorithm has been developed to extract p-DI features for each T cell using a neural network termed as DINet-R and rank the cells by a correlation matrix calculated with the feature vectors of all cells in the same subtype learned by DINet-R. A set of “support cells” was selected for each T cell subtype by its correlation ranking and the two support cell sets were used to divide each subtype into two groups of A and B. With this algorithm, we have demonstrated for the first time the existence of high correlation between the 3D morphology and immunophenotyping of human primary T cells defined by surface CD markers. The results also show the feasibility for development of a label-free, robust, and cost-effective approach to accurately classify white blood cells using the p-DIFC method beyond the five major types in the current protocol of complete blood count.³⁰

MATERIALS AND METHODS

Under a protocol approved by IRB at East Carolina University (ECU), microscopic examinations have been carried out on lymphocytes isolated by centrifugation from peripheral blood samples of clinical patients with non-hematologic disorders and spleen tissues of trauma and otherwise healthy patients. No significant differences in the morphology can be identified in the isolated lymphocytes of these patients by blood smears of fixed cells and confocal images of live cells. Based on these observations, we have performed fluorescence-activated cell sorting (FACS) to isolate T cells for acquisition of p-DI pairs. Fresh spleen tissues of two trauma and otherwise healthy patients were received within hours after surgery from the Department of Pathology and Laboratory Medicine in the Brody School of Medicine of ECU. To obtain splenocytes, a spleen tissue sample was immersed and fragmented with surgical scissors in a dish filled with RPMI-1640 culture media (11875101, Fisher Scientific). A cell suspension was prepared after filtering the fragmented tissue in the RPMI media through a wire screen of 70 μm in hole size, followed by centrifugation at 250g for 10 min. Red blood cells (RBCs) in resuspended cells were then removed by an RBC lysis buffer (00-4333-57, ThermoFisher) and centrifugation. The remaining splenocytes were washed, viability tested by trypan blue staining, which is found to be about 85%, and prepared in 1% BSA in PBS with a pH value of 7.4 as a stock cell suspension with a concentration of 4.7×10^7 cells/mL. For each spleen tissue sample, the suspension of splenocytes with 100 μL in volume was aliquoted into five tubes consisting of four control tubes with cells, respectively, not stained and singly stained by CD3 (CD0304, ThermoFisher), CD4 (MHCD0405), and CD8 (MHCD0801) and one tube with cells triply stained by CD3, CD4, and CD8 for isolation of the two subtypes. The control tubes were used to obtain correct gate settings for scatter and fluorescent channels of the sorter (FACSAria Fusion, BD Biosciences). To increase purity, the sorting of CD4+ and CD8+ T cells was repeated and the collected cells were resuspended to a concentration of about 1×10^6 cells/mL. Multiple measurements of p-DIFC and confocal imaging were performed within 48 h from spleen removal.

For p-DI acquisition, each CD4+ or CD8+ cell suspension sample was pressurized in a sealed tube into a core fluid channel and injected into the flow chamber of a p-DIFC system through a glass nozzle to form a core fluid stream. The schematics of the sample entry port and flow chamber with the core and sheath fluids indicated is presented as Figure S1 of the Supporting Information. A continuous-wave laser beam of $\lambda = 532$ nm in wavelength was linearly polarized in the vertical plane with 45° between the vertical and horizontal directions. The incident beam was focused on the core fluid carrying cells in a single file by hydrodynamic focusing with the sheath fluid through the focal spot around 30 μm in diameter under the laminar flow condition. The scattered light by a moving cell is collected by an imaging unit within a cone of 20.3° in half angle centered in the side direction of 90° from the incident beam direction.³¹ The imaging unit consists of an infinity-corrected 50 \times objective of 0.55 in numerical aperture (378-805-3, Mitutoyo), a narrow-band filter centered at 532 nm, a polarizing beam splitter for separating scattering light into s- and p-polarized components, two tube lenses and CCD cameras (LM075, Lumenera) for p-DI acquisition, and a photomultiplier for triggering the cameras. The unit, with each

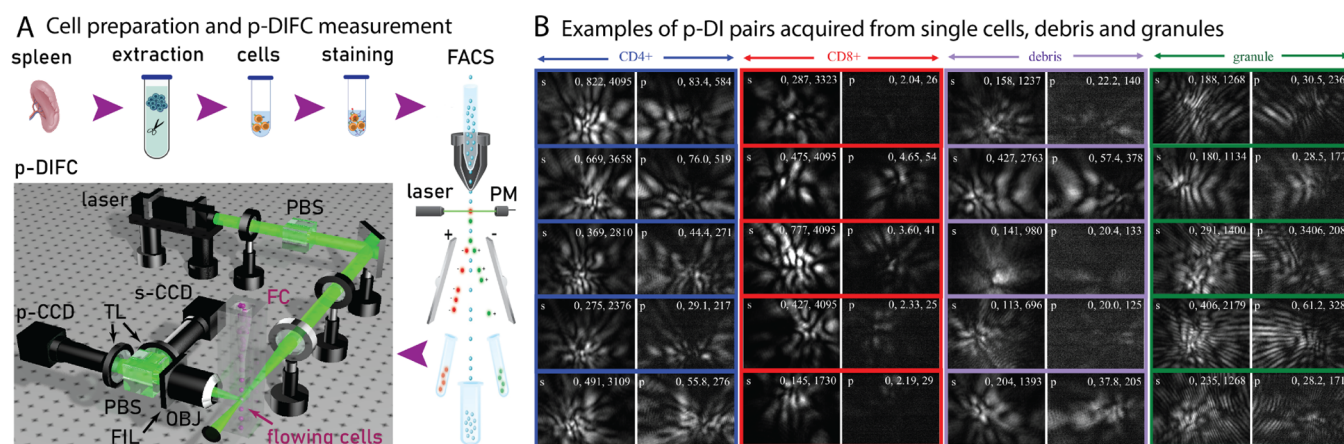


Figure 1. (A) Work flow diagram of cell preparation and p-DI acquisition: FACS = fluorescence-activated cell sorting; PM = photomultiplier; PBS = polarizing beam splitter; FC = flow chamber; OBJ = objective, FIL = 532 nm filter; TL = tube lens; and s- or p-CCD = cameras for imaging s- and p-polarized light. (B) Five examples of p-DI pairs in each class of cells (labeled as CD4+ and CD8+), debris, and granules by manual selection. Each 12-bit diffraction image is marked on the top with light polarization, followed by minimum, average, and maximum pixel intensities.

camera sensor fixed to the focal plane of its tube lens, can be translated away from the focusing position toward the flow chamber to increase the contrast and vary angular field of view by non-conjugate diffraction imaging.^{18,31} The p-DI data were acquired with an off-focus distance set to 80 μm for T cells and camera exposure time to 0.3 ms. Each image of a p-DI pair consists of 640×480 pixels with pixels of 12-bit in depth.

After injection into the flow chamber of an experimental p-DIFC system, either CD4+ or CD8+ T cells in culture medium flows as the core fluid along the vertical direction through the focal spot of an incident laser beam. The acquired p-DI pairs were first preprocessed to remove overexposed and underexposed pairs. The former is defined to be those with one image in a pair having the number of saturated pixels larger than 2% of total pixel number and the latter is defined as those with both images in a pair having average pixel intensity less than 2% of the pixel saturation value. The next step is to identify and remove p-DI pairs by non-cellular particles. Besides cells, the core fluid of cell suspension also contains other particles of cellular debris and granules of aggregated microscopic non-cellular particles, which include powder residues not fully dissolved in the culture media.

RESULTS

Four samples of CD4+ or CD8+ T cells were prepared from spleen tissues and measured over a period of 6 weeks between the two patients using the same p-DIFC system. Figure 1A presents a work flow diagram for cell preparation and p-DI data acquisition. A total of 7755 p-DI pairs were obtained after removing 2220 underexposed p-DI pairs and 6 overexposed ones through preprocessing. Many of the underexposed p-DI pairs were due to dying cells that suffer significant loss of ability to scatter light resulted from reduction of RI heterogeneity by fragmented organelles.³² We have previously shown by simulations of p-DI pairs with different particle models that the acquired and preprocessed data can be divided into three classes of cell, debris, and granule according to their diffraction patterns in which the debris class also include dying cells.^{20,22,32} Guided by these studies, the preprocessed data were manually separated and labeled and verified by two coauthors, which were obviously subjective, to train and test different neural networks to determine an optimized network

architecture. Table 1 shows the numbers of p-DI pairs that were manually divided into the three classes and Figure 1B

Table 1. Distribution of Acquired p-DI Pairs and Preprocessing by DINet-R^a

preprocessing of p-DI data	cells				accuracy (%) ^b
	CD4+	CD8+	debris	granule	
manual labeling	2408	2373	2290	684	
first training of DINet-R	4781				684
prediction by first trained DINet-R	4933	2168	654		95.0 \pm 0.63
second training of DINet-R	2483	2450			
prediction by second trained DINet-R					91.7 \pm 0.91

^aThe ground-truth labels for first and second training were given, respectively, by cells vs debris vs granules and CD4+ vs CD8+. ^bThe average (A_{av}) and standard deviation (A_{std}) values of classification accuracy A were obtained from five values of A on the five test datasets based on the 5-fold cross-validation scheme for training and test.

shows 5 examples for each class of the p-DI pairs of cells, labeled separately by CD markers, debris, and granules. For DNN-based learning, we have combined the two images in each pair into green and red channels of one false-color image as the input data. The two channels were normalized by the same minimum and maximum pixel values of the p-DI pair to preserve the intensity ratio of the two cross-polarized images in the same pair.

Development and First Training of DINet-R for Ternary Classification. The non-local nature of diffraction imaging using the p-DIFC method requires no image segmentation, which fits well to machine learning for extraction of diffraction pattern features. We have modified a previously developed network with different combination of convolutional, pooling layers and residual blocks.^{28,33} The final version of the network architecture was denoted as DINet-R and is illustrated in Figure S2 of the Supporting Information. The DINet-R network was first trained to classify input the p-DI

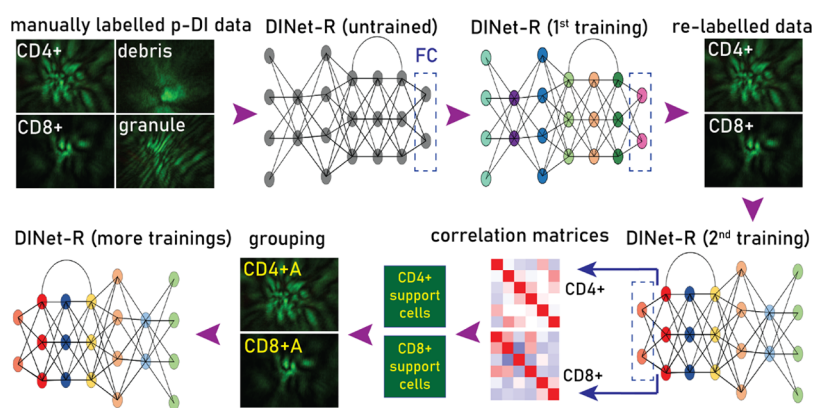


Figure 2. Work flow diagram of training and test of DINet-R for ternary and binary classifications of p-DI data, followed by T cell grouping. The lower row illustrates feature extraction by DINet-R after second training to calculate two symmetric correlation matrices and select support cells for dividing each subtype into A and B groups.

data presented in Figure 1B into three classes of cells, debris, and granules. The same network was subsequently retrained to perform binary classifications of CD4+ versus CD8+ T cells.

The manually labeled p-DI pairs with possible errors are listed in Table 1 and are divided randomly into 5 sets for training and test of DINet-R using a 5-fold cross validation scheme.²⁸ One set was chosen as the held-out test dataset and the rest as the training-validation dataset to perform five rounds of training and test by rotating the test dataset. The trained DINet-R was employed to identify the p-DI pairs that were manually labeled as debris or granules but predicted as cells in each test dataset. These p-DI pairs from the five test datasets were pooled and relabeled as either CD4+ or CD8+ T cells based on which cell sample was used to acquire these p-DI pairs. The upper row of Figure 2 shows the work flow of the first training of DINet-R. Approximately 90% of the p-DI pairs in the final class of cells were those manually labeled as cells and the rest were manually labeled as either debris or granules and relabeled as cells by the trained DINet-R. The average value A_{av} and standard deviation A_{std} of classification accuracy among the three classes of cells, debris, and granules were found to be $95.0 \pm 0.63\%$. The corresponding confusion matrices are presented in Figure S3 of the Supporting Information. Table 1 also includes the numbers of T cells labeled by DINet-R that were taken as the ground-truth labels for the subsequent binary classification in the results presented below.

Correlations between Diffraction Pattern Features and CD Markers. The p-DI pairs of CD4+ and CD8+ T cells in the form of one false-color image for each pair were imported into DINet-R for second training and binary classification of CD4+ versus CD8+ using the same 5-fold scheme. As shown in Table 1, the classification accuracy was found to be $91.7 \pm 0.91\%$ and the corresponding confusion matrices are shown in Figure S4 of the Supporting Information. Even though the above value of A_{av} is not very high, the results suggest the existence of correlations between the T cell subtype defined by CD markers and the diffraction pattern features. Given the T cells' heterogeneity by their diverse functions in each subtype, we strive to develop an algorithm for selection of certain T cells as "support cells" and grouping cells in each subtype by these cells. The purpose of grouping is to gain insights on the relation between the cell morphology as revealed by p-DI features and cell surface molecular profiles. It is expected that support cells for each

subtype exhibit high morphologic correlation among themselves in the same set and hopefully sufficient dissimilarity between the two sets by their p-DI data. Existing methods have been explored for selecting support cells that range from clustering in the features' space by density peaks to various active learning of the input data with noisy labels.^{34–37} None of these methods, however, yielded a notably higher accuracy for binary classification between the two subtypes after grouping by support cells. A new and novel algorithm for objective grouping of T cells in a subtype has been developed by ranking correlations of p-DI features for selection of support cells. Each subtype was divided into two groups by comparing the correlation coefficients against the two sets of support cells for accurate binary classification. The work flow is illustrated in the lower row of Figure 2.

The algorithm starts from the 2560 features used as the input to the FC layer of DINet-R after second training with p-DI pairs of the CD4+ and CD8+ cells listed in Table 1. Let us denote the i th cell in subtype k as x_{ki} , with $k = 1$ for CD4+ and $k = 2$ for CD8+ cells, and the cell can then be represented by a column vector $z(x_{ki})$ of the p-DI features after a z-score normalization. Each vector component was defined by

$$z_l(x_{ki}) = \frac{f_l(x_{ki}) - \mu(x_{ki})}{\sigma(x_{ki})} \quad (1)$$

where $f_l(x_{ki})$ is the l th feature with $l \in [1, L]$ and $L = 2560$, $\mu(x_{ki})$ and $\sigma(x_{ki})$ is respectively, the average and standard deviation value of all features for the cell. The feature vectors of paired cells in subtype k were used to determine a correlation matrix $[r_k]$ as follows

$$[r_k] = \frac{1}{L-1} \begin{pmatrix} z^T(x_{k1}) \\ \dots \\ z^T(x_{kL_k}) \end{pmatrix} (z(x_{k1}) \dots z(x_{kL_k})) \quad (2)$$

where the superscript T refers to transpose operation. Each element r_{kij} of $[r_k]$ is the Pearson correlation coefficient between cell x_{ki} and x_{kj} and thus the matrix is symmetric and of rank given by total number L_k of cells in subtype k with diagonal elements of unit values.

Figure 3 presents a portion of the correlation matrices calculated for the two subtypes, and the complete ones are plotted in Figure S5 of the Supporting Information. The diagrams show clearly that the CD4+ T cells are of significantly

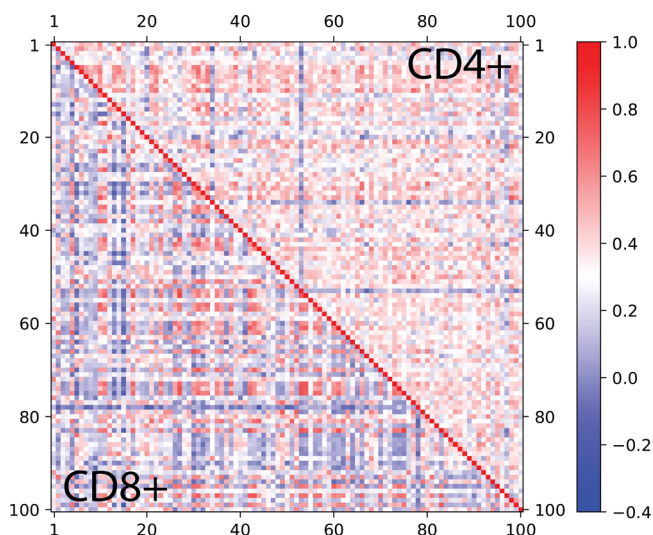


Figure 3. Upper-right or lower-left half of correlation matrices for 100 T cells of CD4 and CD8 subtypes as marked with the axes representing cell indices i and j . The color bar indicates matrix element values given by the Peterson correlation coefficients between two cells.

higher morphologic correlations within their subtype than the CD8+ T cells, which is corroborated by the average and standard deviation values of the Pearson correlation coefficient for all paired cells as 0.356 ± 0.12 for CD4+ and 0.271 ± 0.12 for CD8+ T cells. Each correlation matrix was used to form a set of S_k support cells in two steps with S_k set at 10% of I_k for each subtype.

In the first step, an initial set was created by selecting S_k cells of largest correlation density defined by

$$\rho_{ki} = \sum_{\substack{j=1 \\ (j \neq i)}}^{I_k} H(r_{k,ij} - r_{th}) \quad (3)$$

where $H(x)$ is the Heaviside function with r_{th} as a threshold. The density ρ_{ki} for cell x_{ki} represents the number of cells having correlation coefficients larger than r_{th} within each subtype. The r_{th} value was found to have little effect on the result of initial selection of support cells by varying it from 0.2 to 0.8 and was set to 0.5 for this study. During the second step, an enhanced correlation coefficient R_{ki} was calculated for each cell in subtype k with all cells in the initial support cell set of the subtype, excluding itself, by the following definition

$$R_{ki} = \rho_{ki} \sum_{\substack{j=1 \\ (j \neq i)}}^{S_k} r_{k,ij} \quad (4)$$

The final support cell set was determined by the cells of largest R_{ki} values in subtype k . It is obvious from this procedure that the support cells must exhibit high correlations with each other in the set and with other cells in the same subtype as well in terms of their diffraction feature vectors. Figure 4 presents the combined diffraction images of 20 randomly selected support cells for each subtype and they indeed show high similarity of diffraction patterns within each subtype. More importantly, pattern dissimilarity can be clearly seen between the two subtypes. We also observe that the linear depolarization ratio δ ,

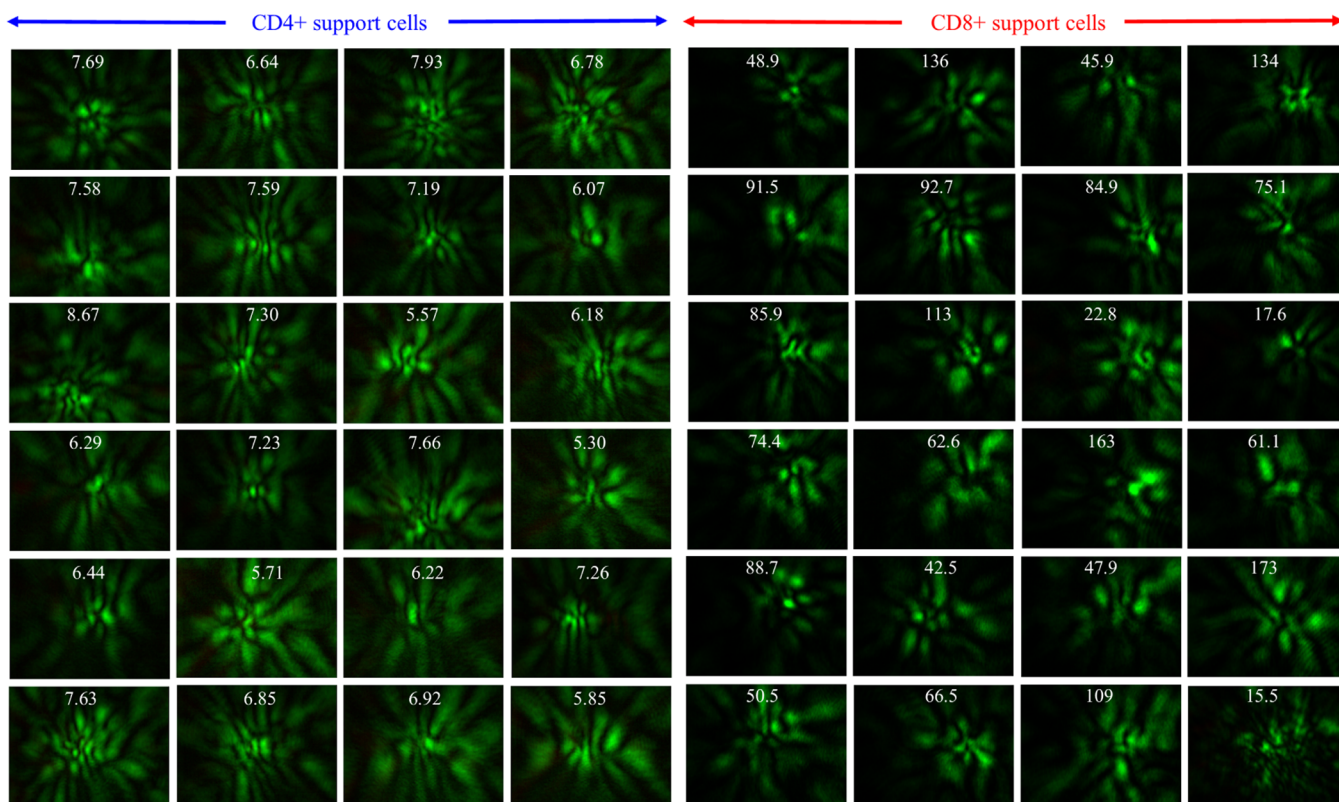


Figure 4. Twenty examples of combined images of p-DI pairs randomly selected from support cells of two T cell subtypes with values of linear depolarization ratio δ marked in each image.

given by the ratio of average pixel intensity of the s-polarized and p-polarized DIs in each pair, differs by an order of magnitude between the two support cell sets.

With the two support cell sets, we divided each T cell subtype into two groups of A and B, respectively. The group A consists of cells having stronger correlation with the support cells in the same subtype k than with support cells in the other subtype, while group B is made of cells having opposite relation. Consequently, two support correlation coefficients of $k = 1$ and 2 were defined for each cell by

$$s_{ki} = \sum_{j=1}^{S_k} r_{k,ij} \quad (5)$$

By comparing the two coefficients of s_{ki} for each cell, each subtype k was divided into group A with $s_{ki} > s_{k'i}$ and k' referring to the other subtype and group B with $s_{ki} \leq s_{k'i}$. Table 2 lists the results of grouping and binary classification for

Table 2. Correlation Grouping and Binary Classifications by DINet-R

results of correlation grouping and binary classification	CD4+ ($k = 1$)		CD8+ ($k = 2$)		accuracy (%) $A_{av} \pm A_{std}$
	A	B	A	B	
grouping by $[r_k]$ with $k = 1$ or 2	2330	153	2121	329	
binary classification: CD4+ A vs CD8+ A	2330		2121		97.3 ± 0.40
binary classification: CD4+ A vs CD4+ B	2330	153			97.1 ± 0.95
binary classification: CD8+ A vs CD8+ B			2121	329	93.4 ± 0.99
binary classification: CD4+ B vs CD8+ A		153	2121		93.6 ± 0.38
binary classification: CD4+ A vs CD8+ B	2330			329	90.0 ± 1.72

paired groups between the two T cell subtypes. Each binary classification took about 2.5 h on one GPU board (GeForce RTX 2060 S, Nvidia) to complete training and test.

Figure 5 plots histograms of linear depolarization ratios δ between the two images in each p-DI pair of the support cell sets, A and B groups of CD4+ and CD8+ T cells. Because the A groups contain the majority of T cells, these results manifest the effectiveness of correlation matrix based support cells to identify those T cells with maximized dissimilarity in

diffraction patterns between the two subtypes defined by surface CD markers, which also result in accurate subtype classification by the p-DI data. It is of interest to note in Figure 5 that cell distributions of the A groups resemble closely to those of the support cell sets between the two subtypes. In contrast, cell distributions of the B groups show opposite behaviors with the CD4+ exhibiting a wider range of δ values than the CD8+ cells. To further confirm these observations, we applied a technique for 2D visualization of imaged T cell distribution according to their feature vectors of 2560 components learned by the DINet-R from p-DI pairs.³⁸ Figure 6A shows the scatter plot of all cells in the two subtypes with

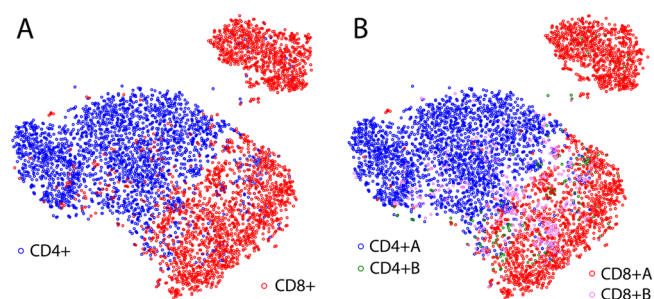


Figure 6. 2D scatter plots of 4933 T cells by application of the dimension reduction technique to the 2560 diffraction features extracted for each cell by DINet-R: (A) CD4+ and CD8+ cells; (B) A and B groups of CD4+ and CD8+ cells.

CD4+ cells presenting clustering distribution tighter than CD8+ T cells. This difference in distributions is, interestingly, reversed in the case of two B groups as illustrated in Figure 6B.

To verify if the total number of the p-DI features can be reduced from $L = 2650$ to obtain a similar performance of binary classification, we have modified the DINet-R structure by adding another fully connected layer after the FC layer. This allowed us to select support cells and group the two T cell subtypes with $L = 1920, 1280,$ and 640 by adjusting the element number in the new FC layer. After the same steps of training and test of the modified DINet-R with the 5-fold cross validation scheme, correlation matrices were calculated to determine correlation ranking, select support cells, and grouping each subtype. The values of A_{av} for binary classification between the two A groups in CD4+ and CD8+ T cells were found to range from 92.9 to 93.5%, which were significantly lower than the case of $L = 2650$. The modified

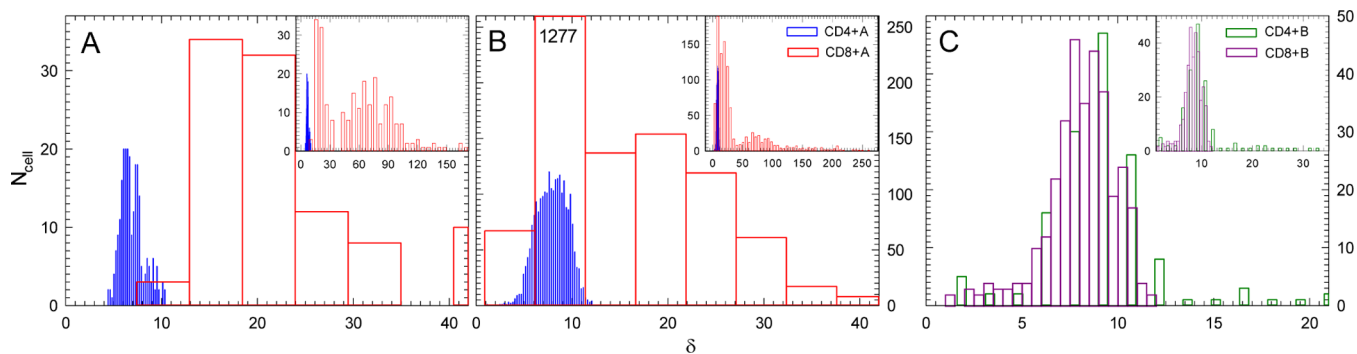


Figure 5. Histograms of 4933 T cells in two subtypes with linear depolarization ratio δ as the bin center value and N_{cell} as the cell number per bin: (A) all support cells; (B) all cells of A groups with the N_{cell} value marked on bin of $\delta = 8.8$ for the CD8+ A group; and (C) all cells of B groups. Insets: same plots on expanded δ scales.

DINet-R architecture and detailed results are presented in Figure S6 and Table S1 of the Supporting Information.

DISCUSSION

Previous studies of the T cell morphology were performed by local imaging, whereas diffraction imaging employed in this study is of non-local nature. The ability to sense each dimension of 3D cell morphology on equal foot by image texture features, with a throughput rate of a few cells per second by the experimental system, enabled us to investigate morphologic correlations among T cells phenotyped by the surface markers of CD4 and CD8 in a way inaccessible before. The algorithm developed through this study combines 2560 diffraction features learned by DINet-R into a feature vector for each imaged cell to obtain the Pearson correlation coefficients with others in each subtype, which was used to form a matrix as a collective view of morphologic correlations. The support cell set selected for each subtype by its correlation matrix exhibits highly similar diffraction patterns within the set and clear distinction against the other set as shown in Figure 4. These results provide convincing evidence on a strong association between the morphology and CD markers for these T cells. Quantitative insights can be gained by examining the distributions of depolarization ratio data in Figure 5 and diffraction feature data in Figure 6. The linear depolarization ratio δ of each p-DI pair depends on the types and spatial distribution of intracellular molecules. Given the polarizations of the incident beam, different δ values indicate different ratios of molecular types to emit side scatter between p- and s-polarized ones by their polarizability affecting RI values.^{20–22} Taken together, these data prove that the support cells and group A of CD4+ T cells exhibit markedly higher morphologic correlation than CD8+ T cells isolated from fresh human splenocytes.

We also note that T cells distribute very differently between the two subtypes in Figures 5 and 6 by comparing the A groups to B groups. The CD4+ cells in group A present high morphologic correlations among each other by their features as illustrated in Figure 5B, while the CD8+ cells in group A show considerable heterogeneity in distribution. The support cells resemble very closely to cells in the A groups. In contrast, the two B groups in Figure 5C display quite similar and heterogeneous distributions that are consistent with the distribution of two B groups shown in Figure 6B. Comparing the data in the above two figures demonstrates clearly that the T cells in the B groups mix well among themselves and also blend well with those in the A groups. The distributions of δ and diffraction feature vectors among the two B groups could be attributed to the existence of CD4/CD8 double positive (DP) T cells in peripheral blood and secondary lymphoid organs of human and other animals.^{39,40} We thus suggest that the T cells in the two B groups are likely the DP T cells with very heterogeneous distributions as revealed in Figures 5 and 6, which have been reported to be the result of re-expression of the CD8 coreceptor on mature CD4+ T cells.⁴⁰ It should be pointed out that further investigations by p-DIFC measurement are needed to test the above hypotheses, which may prepare the ground for exploring the structure–function relation among additional T cell subtypes.

ASSOCIATED CONTENT

Supporting Information

The Supporting Information is available free of charge at <https://pubs.acs.org/doi/10.1021/acs.analchem.1c03337>.

Architecture of DINet-R; schematics of the sample entrance port and flow chamber; confusion matrices of tertiary classification on three classes of cell, debris, and granules and binary classification on CD4+ and CD8+ T cells by DINet-R; correlation matrices of all T cells in the subtypes of CD4+ and CD8+ with feature vectors of $L = 2560$ components; architecture of the modified DINet-R; and grouping results and classification accuracy with feature vectors of $L = 1920, 1280,$ and 640 components (PDF)

AUTHOR INFORMATION

Corresponding Author

Xin-Hua Hu – Department of Physics, East Carolina University, Greenville, North Carolina 27858, United States; Institute for Advanced Optics, Hunan Institute of Science and Technology, Yueyang, Hunan 414006, China; orcid.org/0000-0002-4353-9028; Email: hux@ecu.edu

Authors

Lin Zhao – Institute for Advanced Optics, Hunan Institute of Science and Technology, Yueyang, Hunan 414006, China; Department of Physics, East Carolina University, Greenville, North Carolina 27858, United States; School of Information Science & Technology, Hunan Institute of Science and Technology, Yueyang, Hunan 414006, China; orcid.org/0000-0003-3514-4330

Liwen Tang – Institute for Advanced Optics, Hunan Institute of Science and Technology, Yueyang, Hunan 414006, China; School of Information Science & Technology, Hunan Institute of Science and Technology, Yueyang, Hunan 414006, China

Marion S. Greene – Department of Physics, East Carolina University, Greenville, North Carolina 27858, United States

Yu Sa – Department of Biomedical Engineering, Tianjin University, Tianjin 300072, China

Wenjin Wang – Institute for Advanced Optics, Hunan Institute of Science and Technology, Yueyang, Hunan 414006, China; School of Physics & Electronic Science, Hunan Institute of Science and Technology, Yueyang, Hunan 414006, China

Jiahong Jin – Institute for Advanced Optics, Hunan Institute of Science and Technology, Yueyang, Hunan 414006, China; Department of Physics, East Carolina University, Greenville, North Carolina 27858, United States; School of Physics & Electronic Science, Hunan Institute of Science and Technology, Yueyang, Hunan 414006, China

Heng Hong – Department of Pathology and Comparative Medicine, Wake Forest School of Medicine, Wake Forest University, Winston-Salem, North Carolina 27109, United States

Jun Q. Lu – Department of Physics, East Carolina University, Greenville, North Carolina 27858, United States; Institute for Advanced Optics, Hunan Institute of Science and Technology, Yueyang, Hunan 414006, China

Complete contact information is available at: <https://pubs.acs.org/10.1021/acs.analchem.1c03337>

Notes

The authors declare no competing financial interest.

ACKNOWLEDGMENTS

We thank Prof. Kymberly M. Gowdy, Dr. Douglas A. Weidner, and Prof. Li V. Yang for their help on extraction of splenocytes and sorting of T cells. This work was supported in part by National Institutes of Health of grant no. 1S10OD021615-01, and W.W. acknowledges grant support of #18B348 by the Education Department of Hunan Province and #2020JJS219 by the Science and Technology Department of Hunan Province, China.

REFERENCES

- (1) Judokusumo, E.; Tabdanov, E.; Kumari, S.; Dustin, M. L.; Kam, L. C. *Biophys. J.* **2012**, *102*, L5–L7.
- (2) Karandikar, S. H.; Zhang, C.; Meiyappan, A.; Barman, I.; Finck, C.; Srivastava, P. K.; Pandey, R. *Anal. Chem.* **2019**, *91*, 3405–3411.
- (3) Roath, S.; Newell, D.; Polliack, A.; Alexander, E.; Lin, P.-S. *Nature* **1978**, *273*, 15–18.
- (4) Strokotov, D. I.; Yurkin, M. A.; Gilev, K. V.; van Bockstaele, D. R.; Hoekstra, A. G.; Rubtsov, N. B.; Maltsev, V. P. *J. Biomed. Opt.* **2009**, *14*, 064036.
- (5) Kono, M.; Takagi, Y.; Kawauchi, S.; Wada, A.; Morikawa, T.; Funakoshi, K. *Cytometry, Part A* **2013**, *83A*, 396–402.
- (6) Yakimov, B. P.; Gogoleva, M. A.; Semenov, A. N.; Rodionov, S. A.; Novoselova, M. V.; Gayer, A. V.; Kovalev, A. V.; Bernakevich, A. I.; Fadeev, V. V.; Armaganov, A. G.; Drachev, V. P.; Gorin, D. A.; Darvin, M. E.; Shcheslavskiy, V. I.; Budylin, G. S.; Priezhev, A. V.; Shirshin, E. A. *Biomed. Opt. Express* **2019**, *10*, 4220–4236.
- (7) Maecker, H. T.; McCoy, J. P.; Nussenblatt, R. *Nat. Rev. Immunol.* **2012**, *12*, 191–200.
- (8) Fagnoni, F. F.; Vescovini, R.; Passeri, G.; Bologna, G.; Pedrazzoni, M.; Lavagetto, G.; Casti, A.; Franceschi, C.; Passeri, M.; Sansoni, P. *Blood* **2000**, *95*, 2860–2868.
- (9) Carrara, S.; Vincenti, D.; Petrosillo, N.; Amicosante, M.; Girardi, E.; Goletti, D. *Clin. Infect. Dis.* **2004**, *38*, 754–756.
- (10) Zhu, J.; Paul, W. E. *Cell Res.* **2010**, *20*, 4–12.
- (11) Yang, Y.; Kohler, M. E.; Chien, C. D.; Sauter, C. T.; Jacoby, E.; Yan, C.; Hu, Y.; Wanhainen, K.; Qin, H.; Fry, T. J. *Sci. Transl. Med.* **2017**, *9*, No. eaag1209.
- (12) Alter, G.; Yu, J.; Liu, J.; Chandrashekar, A.; Borducchi, E. N.; Tostanoski, L. H.; McMahan, K.; Jacob-Dolan, C.; Martinez, D. R.; Chang, A.; Anioke, T.; Lifton, M.; Nkolola, J.; Stephenson, K. E.; Atyeo, C.; Shin, S.; Fields, P.; Kaplan, I.; Robins, H.; Amanat, F.; et al. *Nature* **2021**, *596*, 268–272.
- (13) Potter, A.; Kim, C.; Gollahon, K. A.; Rabinovitch, P. S. *Cell. Immunol.* **1999**, *193*, 36–47.
- (14) Schnell, U.; Dijk, F.; Sjollem, K. A.; Giepmans, B. N. G. *Nat. Methods* **2012**, *9*, 152–158.
- (15) Zhang, Y.; Feng, Y.; Justus, C. R.; Jiang, W.; Li, Z.; Lu, J. Q.; Brock, R. S.; McPeck, M. K.; Weidner, D. A.; Yang, L. V.; Hu, X.-H. *Integr. Biol.* **2012**, *4*, 1428–1436.
- (16) Yoon, J.; Kim, K.; Park, H.; Choi, C.; Jang, S.; Park, Y. *Biomed. Opt. Express* **2015**, *6*, 3865–3875.
- (17) Jacobs, K. M.; Lu, J. Q.; Hu, X.-H. *Opt. Lett.* **2009**, *34*, 2985–2987.
- (18) Jacobs, K. M.; Yang, L. V.; Ding, J.; Ekpenyong, A. E.; Castellone, R.; Lu, J. Q.; Hu, X.-H. *J. Biophot.* **2009**, *2*, 521–527.
- (19) Sa, Y.; Feng, Y.; Jacobs, K. M.; Yang, J.; Pan, R.; Gkigkitzis, I.; Lu, J. Q.; Hu, X.-H. *Cytometry, Part A* **2013**, *83*, 1027–1033.
- (20) Zhang, J.; Feng, Y.; Jiang, W.; Lu, J. Q.; Sa, Y.; Ding, J.; Hu, X.-H. *Opt. Express* **2016**, *24*, 366–377.
- (21) Wang, S.; Liu, J.; Lu, J. Q.; Wang, W.; Al-Qaysi, S. A.; Xu, Y.; Jiang, W.; Hu, X. H. *J. Biophot.* **2019**, *12*, No. e201800287.
- (22) Liu, J.; Xu, Y.; Wang, W.; Wen, Y.; Hong, H.; Lu, J. Q.; Tian, P.; Hu, X.-H. *J. Biophot.* **2020**, *13*, No. e202000036.
- (23) Dong, K.; Feng, Y.; Jacobs, K. M.; Lu, J. Q.; Brock, R. S.; Yang, L. V.; Bertrand, F. E.; Farwell, M. A.; Hu, X.-H. *Biomed. Opt. Express* **2011**, *2*, 1717–1726.
- (24) Feng, Y.; Zhang, N.; Jacobs, K. M.; Jiang, W.; Yang, L. V.; Li, Z.; Zhang, J.; Lu, J. Q.; Hu, X.-H. *Cytometry, Part A* **2014**, *85*, 817–826.
- (25) Yang, X.; Feng, Y.; Liu, Y.; Zhang, N.; Lin, W.; Sa, Y.; Hu, X.-H. *Biomed. Opt. Express* **2014**, *5*, 2172–2183.
- (26) Jiang, W.; Lu, J. Q.; Yang, L. V.; Sa, Y.; Feng, Y.; Ding, J.; Hu, X.-H. *J. Biomed. Opt.* **2015**, *21*, 071102.
- (27) Wang, H.; Feng, Y.; Sa, Y.; Lu, J. Q.; Ding, J.; Zhang, J.; Hu, X.-H. *Pattern Recogn.* **2017**, *61*, 234–244.
- (28) Jin, J.; Lu, J. Q.; Wen, Y.; Tian, P.; Hu, X.-H. *J. Biophot.* **2020**, *13*, No. e201900242.
- (29) Attaf, M.; Legut, M.; Cole, D. K.; Sewell, A. K. *Clin. Exp. Immunol.* **2015**, *181*, 1–18.
- (30) Buttarello, M.; Plebani, M. *Am. J. Clin. Pathol.* **2008**, *130*, 104–116.
- (31) Pan, R.; Feng, Y.; Sa, Y.; Lu, J. Q.; Jacobs, K. M.; Hu, X.-H. *Opt. Express* **2014**, *22*, 31568–31574.
- (32) Zhang, J.; Feng, Y.; Moran, M. S.; Lu, J. Q.; Yang, L. V.; Sa, Y.; Zhang, N.; Dong, L.; Hu, X.-H. *Opt. Express* **2013**, *21*, 24819–24828.
- (33) He, K.; Zhang, X.; Ren, S.; Sun, J. *The IEEE Conference on Computer Vision and Pattern Recognition (CVPR)*; IEEE: Las Vegas, Nevada, USA, 2016; pp 770–778.
- (34) Rodriguez, A.; Laio, A. *Science* **2014**, *344*, 1492–1496.
- (35) Lee, K.; He, X.; Zhang, L.; Yang, L. *IEEE/CVF Conference on Computer Vision and Pattern Recognition*; IEEE: Salt Lake City, UT, USA, 2018; pp 5447–5456.
- (36) Han, J.; Luo, P.; Wang, X. *IEEE/CVF International Conference on Computer Vision (ICCV)*; IEEE: Seoul, Korea, 2019; pp 5137–5146.
- (37) Northcutt, C.; Jiang, L.; Chuang, I. J. *Artif. Intell. Res.* **2021**, *70*, 1373–1411.
- (38) van der Maaten, L.; Hinton, G. J. *Mach. Learn. Res.* **2008**, *9*, 2579–2605.
- (39) Zuckermann, F. A. *Vet. Immunol. Immunopathol.* **1999**, *72*, 55–66.
- (40) Overgaard, N. H.; Jung, J.-W.; Steptoe, R. J.; Wells, J. W. J. *Leukoc. Biol.* **2015**, *97*, 31–38.